Contents lists available at ScienceDirect

Applied Catalysis B: Environment and Energy

Alkaline earth metal promoted hydrogen production from ammonia decomposition over Ni/La$_2$O$_3$-based catalysts

Xiao-Yu Guo [a], Jun-Hao Wang [a], Qian Zhang [a], Ting-Zhou Li [a], Hao Dong [a], Chun-Jiang Jia [b], Chen Li [a,*], Ya-Wen Zhang [a,*]

[a] *Beijing National Laboratory for Molecular Sciences, College of Chemistry and Molecular Engineering, Peking University, Beijing 100871, China*
[b] *Key Laboratory for Colloid and Interface Chemistry, Key Laboratory of Special Aggregated Materials, School of Chemistry and Chemical Engineering, Shandong University, Jinan 250100, China*

ARTICLE INFO

ABSTRACT

The addition of appropriate promoters can modulate the chemical characteristics of heterogeneous catalysts so as to improve and optimize their catalytic performance. Here, we introduced SrO as both a support and a promoter to optimize the activity of Ni/La$_2$O$_3$-based catalysts for the ammonia decomposition reaction. A series of La$_{1-x}$Sr$_x$NiO$_{3-\delta}$-600H$_2$ catalysts were prepared by reducing La$_{1-x}$Sr$_x$NiO$_{3-\delta}$ (x = 0, 0.2, 0.33, 0.5, 0.67, 0.8, and 1) precursors under a H$_2$/N$_2$ atmosphere. The La$_{0.5}$Sr$_{0.5}$NiO$_{3-\delta}$-600H$_2$ catalyst with a proper amount of Sr exhibited outstanding ammonia decomposition conversion rate (87.7%) and hydrogen production rate (29.4 mmol·g$_{cat}^{-1}$·min^{-1}) at 550 °C with a GHSV of 30,000 mL·g$_{cat}^{-1}$·h^{-1}. The presence of Sr induced the Ni species to be situated in a more electro-negative environment, thus facilitating the recombination of N atoms and N$_2$ desorption; whereas Ni nanoparticles could be evenly dispersed by La$_2$O$_3$, which rendered the catalyst with high stability. Briefly, the synergistic effect of Sr increasing electron density of Ni species and La$_2$O$_3$ stabilizing Ni nanoparticles has greatly enhanced the catalytic performance. This work has demonstrated a new variety of promising noble metal-free catalysts toward the eventual application in hydrogen production from ammonia decomposition reaction.

1. Introduction

Worldwide demand for hydrogen energy has grown rapidly. However, the storage and utilization of hydrogen continue to present significant difficulties. As a hydrogen carrier, ammonia has the advantages of high production, high hydrogen content (17.8 wt%), low storage pressure, and long-term storage stability [1–4]. Catalytic ammonia decomposition can *in situ* supply high-purity hydrogen to proton exchange membrane fuel cells [5], avoiding poisoning Pt electrodes in the cells. The basic steps of ammonia decomposition for H$_2$ production are shown in Eqs. 1–6. Ganley et al. [6] evaluated the catalytic activity of various metals in the ammonia decomposition reaction and discovered that the activity followed the order of Ru > Ni > Rh > Co > Ir > Fe >> Pt > Cr > Pd > Cu >> Te, Se, Pb. Ruthenium is the most effective metal for catalyzing ammonia decomposition [7–9]. However, limited by the cost of noble metals, it is of crucial importance to develop efficient noble metal-free catalysts. Although Fe-based catalysts perform exceptionally well in the ammonia synthesis reaction [10–13], their activity in the

ammonia decomposition reaction is only fair [14–16]. In contrast, Co and Ni-based catalysts have attracted great attention because of their lower price than Ru-based catalysts and higher activity than Fe-based catalysts [17,18]. However, existing Co and Ni-based catalysts are still less active at low temperatures. Thus, it is urgent to adopt effective strategies to promote their activity for hydrogen production from ammonia.

$$NH_3 + * \rightleftharpoons NH_3* \qquad (1)$$

$$NH_3* + * \rightleftharpoons NH_2* + H* \qquad (2)$$

$$NH_2* + * \rightleftharpoons NH* + H* \qquad (3)$$

$$NH* + * \rightleftharpoons N* + H* \qquad (4)$$

$$N* + N* \rightleftharpoons N_2 + 2* \qquad (5)$$

$$H* + H* \rightleftharpoons H_2 + 2* \qquad (6)$$

* Corresponding authors.
E-mail addresses: chenlichem@pku.edu.cn (C. Li), ywzhang@pku.edu.cn (Y.-W. Zhang).

So far, a variety of strategies have been used to improve the activity of ammonia decomposition catalysts, such as (i) designing bimetallic catalysts [18,19], (ii) constructing active interfaces [20], (iii) optimizing support composition [16,17,21], (iv) adopting atmosphere treatment [22], and (v) adding basic promoters [18], among which (iii) and (v) are common effective strategies [21,23,24]. Recombination and desorption of nitrogen (Eq. 5) is generally considered to be the rate-determining step in the ammonia decomposition reaction. The basic promoters are typically used as electron donors [25], which can transfer electrons to the metals to weaken metal-nitrogen bonds and facilitate nitrogen desorption [2]. Besides, the high basicity is necessary for the support of the ammonia decomposition catalysts. As reported in the literature, the basic sites formed on the surface of O^{2-} can donate electrons to the active metal [21].

In the ammonia decomposition reaction, the supported metal catalysts are usually used to anchor the active metal [26–28], which not only reduces the consumption amount of metal but also improves the activity and stability of the catalysts. Since the intrinsic activity of Co and Ni-based catalysts is much lower than that of noble metals such as Ru, the loading amount of the former species is usually much higher than that of the latter to achieve outstanding activity [16,18,29]. Impregnation is the simplest and most widely used method for preparing supported metal catalysts [30,31]. Although this method is fairly facile, owing to the weak metal-support interaction, the active metal tends to migrate and further aggregate under harsh reaction conditions [32–34]. Recently, perovskite ABO_3 phases as the precursors are used to obtain highly dispersed supported metallic nanoparticles with large loading amounts by reduction treatment [35–37]. The 'A-site' of ABO_3 is usually the lanthanide or alkaline earth metals, whereas the transition metals typically occupy the 'B-site' [38]. When treated under the reduction atmosphere, the transition metal at the 'B-site' will be exsolved from the perovskite lattice and form metal nanoparticles loaded on the surface of oxides [39,40]. In addition, both 'A' and 'B' sites can be replaced by foreign cations to enrich the composition and properties of the catalysts [41–43]. $LaNiO_3$, a typical ABO_3 perovskite phase, has been extensively studied as a precursor for the preparation of highly dispersed supported metal catalysts [36]. The substitution of 'La^{3+}' in $LaMO_3$ by 'Sr^{2+}' has been investigated in dry reforming of methane (DRM) [38,41]. Nevertheless, the effect of alkaline earth metal substitution has not been systematically studied in ammonia decomposition reaction.

Herein, we prepared a new variety of Ni/La_2O_3-based catalysts ($La_{1-x}Sr_xNiO_{3-\delta}-600H_2$ catalysts) with SrO as a promoter by reducing oxide precursors ($La_{1-x}Sr_xNiO_{3-\delta}$) obtained from '$La^{3+}$' in $LaNiO_3$ substituted by 'Sr^{2+}'. The as-prepared $La_{0.5}Sr_{0.5}NiO_{3-\delta}-600H_2$ catalyst with a proper amount of Sr exhibited excellent catalytic performance in ammonia decomposition reaction, with an ammonia conversion rate of nearly 90% and a hydrogen formation rate of 29.4 mmol·g_{cat}^{-1}·min^{-1} at 550 °C. Various characterizations suggested that the addition of Sr not only increased the electron density of the active metal to promote the recombination of N adatoms and N_2 desorption, but also facilitated the reduction of the nickel species in oxide precursors that resulted in generating larger Ni nanoparticles and decreasing the active site numbers. The combined effects enabled $La_{0.5}Sr_{0.5}NiO_{3-\delta}-600H_2$ to display exceptional catalytic activity. In contrast, $La_{0.2}Sr_{0.8}NiO_{3-\delta}-600H_2$ and $SrNiO_{3-\delta}$-600H_2 with higher Sr content became less active. This work provided a feasible strategy for constructing efficient ammonia decomposition catalysts using alkaline earth metal promoters.

2. Experimental

2.1. Materials

$La(NO_3)_3·6H_2O$ (99.9%) was purchased from Shanghai Macklin Biochemical Co., Ltd. $Sr(NO_3)_2$ (A.R.) was purchased from Beijing Xinhua Chemical Reagent Factory. $Ni(NO_3)_2·6H_2O$ (A.R.) was purchased from Beijing Yili Fine Chemicals Co., Ltd. Citric acid monohydrate

($C_6H_8O_7·H_2O$, A.R.) was purchased from Beijing Chemical Works. All reagents were used directly without further purification. High-purity NH_3 (99.999%), 10% NH_3/He, 10% H_2/N_2, and 5% H_2/Ar were purchased from Beijing Haike Yuanchang Practical Gases Corporation. High-purity H_2 (99.999%) was purchased from Beijing AP BAIF Gases Industry Co., Ltd.

2.2. Catalyst preparation

The $La_{1-x}Sr_xNiO_{3-\delta}$ (x = 0, 0.2, 0.33, 0.5, 0.67, 0.8, and 1) oxide precursors were prepared by the sol-gel method. In brief, the stoichiometric amounts of metal nitrates ($La(NO_3)_3·6H_2O$, $Sr(NO_3)_2$, and $Ni(NO_3)_2·6H_2O$) were dissolved in deionized water. The citric acid monohydrate as the complexing agent was added to the mixture (the molar ratio of citric acid monohydrate to the total metal is 1.5). Then, the mixed solution was heated to 70 °C under continuous stirring until a sticky gel was formed. To evaporate the excess water, the gel was transferred to the oven for drying at 120 °C. Following drying, the samples were calcined at 700 °C for 4 h with a temperature ramping rate of 5 °C/min to obtain oxide precursors.

The oxides were reduced at 600 °C for 4 h in the 10% H_2/N_2 in a tube furnace to obtain the final catalysts, which were named as $La_{1-x}Sr_xNiO_{3-\delta}-600H_2$. In addition, $La_{1-x}Sr_xNiO_{3-\delta}-700H_2$ and $La_{1-x}Sr_xNiO_{3-\delta}-800H_2$ were prepared by reducing $La_{1-x}Sr_xNiO_{3-\delta}$ oxide precursors at 700 °C and 800 °C, respectively.

2.3. Characterization of catalysts

Scanning electron microscopy (SEM) was performed on a scanning electron microscope (S-4800, Hitachi, Japan). Transmission electron microscopy (TEM), high-resolution transmission electron microscopy (HRTEM), high-angle annular dark field scanning transmission electron microscopy (HADDF-STEM), and energy dispersive X-ray spectroscopy (EDS) element mapping were performed on a transmission electron microscope (JEM-2100F, JEOL, Japan) at 200 kV.

The powder X-ray diffraction (XRD) measurement was carried out on a D2-PHASER (Bruker, Germany) with Cu Kα radiation (λ = 1.54184 Å). The metal loading amounts of all catalysts were analyzed by inductively coupled plasma objective emission spectroscopy (ICP-OES) on a Profile Spec ICP-OES spectrometer (Prodigy 7, Leeman, USA). The N_2 adsorption-desorption test was operated on a Quantachrome at 77 K. Before the measurement, the catalysts were first degassed at 120 °C for 3 h under vacuum. The specific surface area of catalysts was obtained according to the multipoint Brunauer-Emmett-Teller (BET) method.

The *ex-situ* and *quasi-in situ* X-ray photoelectron spectroscopy (XPS) results were obtained on an Axis Ultra XPS spectrometer (Kratos, U.K.) with an Al Kα X-ray radiation source. The binding energies were calibrated by the C 1 s peak (284.8 eV). For *quasi-in situ* XPS, the samples were first reduced in a H_2 flow at 600 °C for 1 h and then catalyzed the NH_3 decomposition reaction at 550 °C for 1 h, followed by cooling to room temperature under the Ar flow. The catalysts were encapsulated in the Ar atmosphere-protected quartz tube and then transferred to a glovebox for the XPS measurement preparation without exposure to air. The Ni K edge XANES analyses were collected on the 1W1B beamline of Beijing Synchrotron Radiation Facility.

In situ diffusion reflectance infrared Fourier transform spectroscopy (DRIFTS) was performed using a Bruker TENSOR 27 spectrometer. Before the measurements, the catalysts were first activated under a 5% H_2/Ar flow at 450 °C for 30 min and then exposed to He to remove adsorbed species, followed by cooling to room temperature. Before *in situ* characterization, the background spectrum was detected under a He flow and subtracted automatically in subsequent scans. The spectrum was recorded and superimposed 60 times in the fast Fourier transform mode from 50 to 450 °C under a 10% NH_3/He flow.

Temperature-programmed H_2 reduction (H_2-TPR) was conducted on a Tianjin Xianquan TP5080 multi-function adsorption instrument with a
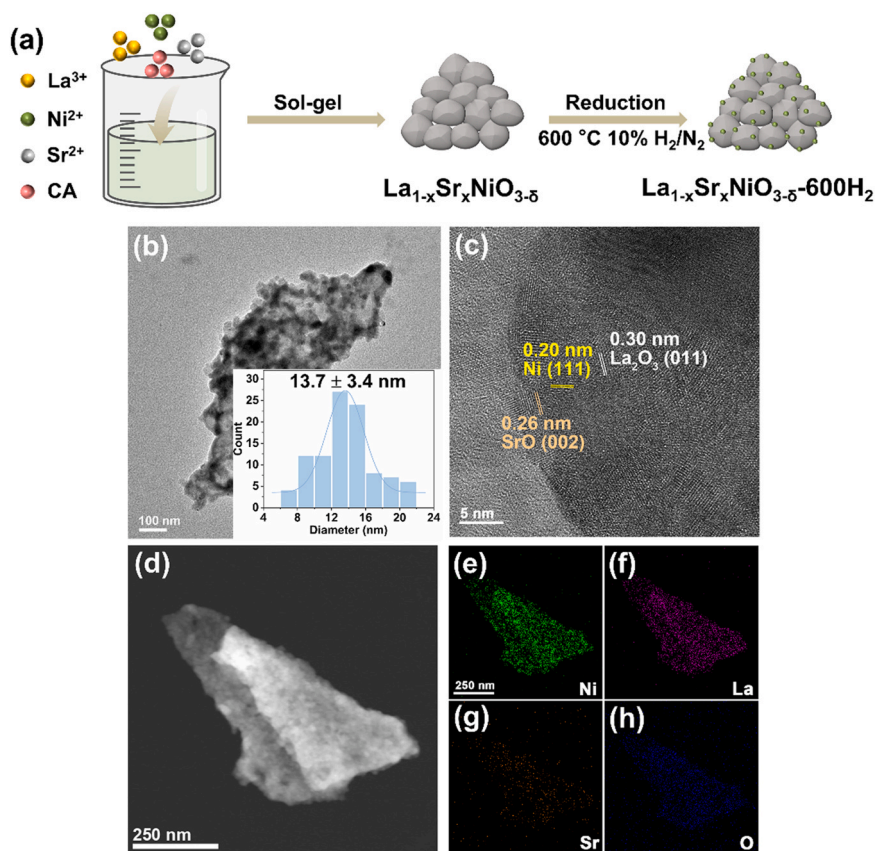
Fig. 1. (a) Schematic illustration of the synthetic process for the catalysts. (b) TEM image (the inset shows the histogram of Ni particle size distribution, based on the statistical analyses of 100 particles), (c) HRTEM image, (d) HADDF-STEM image, and (e-h) EDS elemental mappings of $La_{0.5}Sr_{0.5}NiO_{3-\delta}$-600H$_2$ catalyst.

thermal conductivity detector (TCD). In brief, 50 mg of the sample was first exposed to a He flow at 150 °C for 1 h and then reduced from 50 to 800 °C under a 5% H$_2$/Ar flow at a rate of 10 °C/min. The Temperature-programmed CO$_2$ desorption (CO$_2$-TPD) was performed on a Quantachrome autosorb-iQ instrument. The catalysts were first reduced by 5% H$_2$/Ar at 600 °C for 1 h, and then exposed to a He flow. After cooling down, the catalysts were purged with a 10% CO$_2$/Ar flow for 1 h. After removing the physical adsorption CO$_2$ by a He flow, CO$_2$ desorption was achieved from 50 °C to 1000 °C at a ramp rate of 10 °C/min under a He flow. The mass spectrometer was used to monitor the signal of CO$_2$ (m/z = 44).

Density functional theory (DFT) calculations were performed using the Vienna Ab initio Simulation Package (VASP) [44]. The exchange-correlation functional was treated with the Perdew-Burke-Ernzerhof (PBE) [45] functional and the plane-wave basis set was used with the projector augmented-wave (PAW) [46] method, with cutoff energy of 450 eV. The Brillouin zone was sampled on a 2×2×1 Monkhorst-Pack k-point mesh. The energy convergence criteria were set to be 10^{-4} eV and in the geometric optimization the force tolerance was set to be 0.05 eV/Å. To simulate the $La_{0.5}Sr_{0.5}NiO_{3-\delta}$-600H$_2$ catalyst, we have constructed the structure model of Ni loaded on Sr-doped La$_2$O$_3$ cluster ($La_6Sr_2O_{11}$). According to HRTEM image, (011) lattice planes of La$_2$O$_3$ and $La_6Sr_2O_{11}$ were selected to build the 4×2 surface supercell slab model. The vacuum layer of each unit cell was 20 Å. By the convergence test results, the atoms of the bottom two layers were fixed, and those of the top one layer were relaxed. Vaspkit was used to generate several calculation files [47].

2.4. Catalytic tests

The ammonia decomposition reaction activity was evaluated in a

fixed-bed reactor at atmospheric pressure. A total of 30 mg of the catalysts was diluted with 500 mg of 40–70 mesh quartz sand and placed in a quartz tube. Before the ammonia decomposition reaction, the catalysts were activated in a H$_2$ flow at 600 °C for 1 h and cooled to 350 °C. Then pure NH$_3$ (15 mL/min) was fed into the reactor with the temperature programming from 350 to 600 °C at a step of 50 °C. The NH$_3$ conversion rate and H$_2$ formation rate were analyzed using an online gas chromatograph (GC9790Plus, Fuli). The stability of the catalyst was tested at 550 °C for 48 h. For the kinetic tests, the apparent activation energy was obtained by controlling the NH$_3$ conversion below 15% at different temperatures.

3. Results and discussion

As shown in Fig. 1a, we prepared the oxide precursors through the sol-gel method and then reduced the precursors under a 10% H$_2$/N$_2$ atmosphere to obtain the final catalysts. The catalysts with different atomic ratios of La, Sr, and Ni (1: 0: 1, 0.5: 0.5: 1, 0.2: 0.8: 1, and 0: 1: 1) were named as LaNiO$_{3-\delta}$-600H$_2$, $La_{0.5}Sr_{0.5}NiO_{3-\delta}$-600H$_2$, $La_{0.2}Sr_{0.8}NiO_{3-\delta}$-600H$_2$, and SrNiO$_{3-\delta}$-600H$_2$, respectively. The XRD patterns showed that the LaNiO$_{3-\delta}$ was referred to as the LaNiO$_3$ perovskite phase (Fig. S1a). However, the substitution of 'A-site' by the Sr element destroyed the ABO$_3$ perovskite structure. After being treated under the reduction atmosphere, the Ni species in the oxide precursors were reduced and loaded on oxide supports (Fig. S1b) to form the supported metal catalysts. Metallic Ni (JCPDS No. 01–087–0712), La$_2$O$_3$ (JCPDS No. 01–073–2141), and SrO (JCPDS No. 96–900–8728) were observed from the XRD patterns of catalysts. For the LaNiO$_{3-\delta}$-600H$_2$, the diffraction peaks belonging to metallic Ni and La$_2$O$_3$ were observed. $La_{0.5}Sr_{0.5}NiO_{3-\delta}$-600H$_2$ and $La_{0.2}Sr_{0.8}NiO_{3-\delta}$-600H$_2$ consisted of metallic Ni, SrO, and La$_2$O$_3$. As for the SrNiO$_{3-\delta}$-600H$_2$, there were diffraction

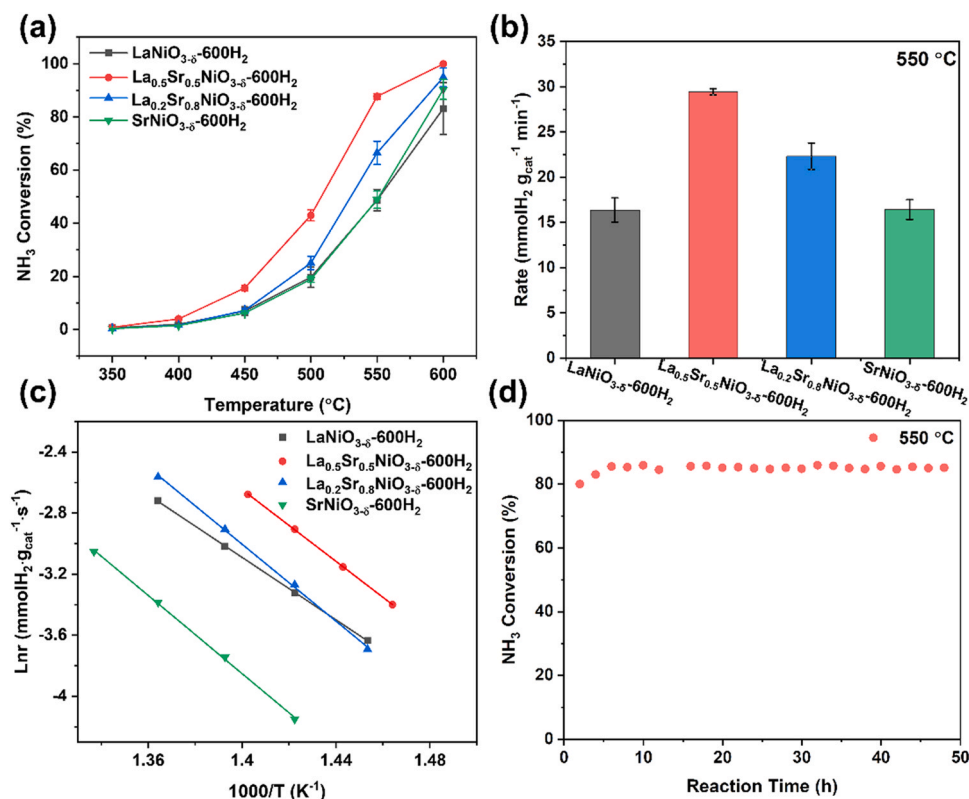**Fig. 2.** Catalytic performance and kinetic tests at a GHSV of 30,000 mL·g_{cat}^{-1}·h^{-1}. (a) NH$_3$ conversion rate over catalysts. (b) The hydrogen production rate over catalysts at 550 °C. (c) Arrhenius plots over catalysts. (d) Stability test over La$_{0.5}$Sr$_{0.5}$NiO$_{3-\delta}$-600H$_2$ at 550 °C.

peaks attributed to metallic Ni and SrO. If considering the existence of Sr in the form of SrO in the sample after reduction, along with the high dispersity of Sr elements as shown in the EDS elemental mappings of the La$_{0.5}$Sr$_{0.5}$NiO$_{3-\delta}$-600H$_2$ catalyst (Fig. 1g), it was likely that a quite small portion of SrO was also doped in La$_2$O$_3$, with referring to previous studies [48–50]. According to the results of ICP-OES (Table S1), the Ni loading amounts of the catalysts were determined to be 25.5, 25.6, 26.8, and 28.6 wt%, respectively. The atomic ratios of La to Sr for La$_{0.5}$Sr$_{0.5}$NiO$_{3-\delta}$-600H$_2$ and La$_{0.2}$Sr$_{0.8}$NiO$_{3-\delta}$-600H$_2$ were quantified as 0.92 and 0.24, respectively, which was consistent with the feed ratio. SEM (Fig. S2) and TEM (Fig. 1b and Fig. S3-S5a) images showed that the catalysts consisted of stacked nanoparticles. The sizes of Ni nanoparticles for the four catalysts were around 8.5, 13.7, 22.7, and 35.0 nm, respectively. As shown in the HRTEM images (Fig. 1c and Fig. S3-S5b), the exposed lattice fringes of 0.20 nm were observed on all catalysts, which could be identified as the (111) lattice plane of the metal Ni, consistent with the diffraction peaks of metal Ni in the XRD characterization (Fig. S1b). In addition, the lattice fringes with values of 0.30 nm and 0.26 nm were observed (Fig. 1c) in the La$_{0.5}$Sr$_{0.5}$NiO$_{3-\delta}$-600H$_2$ catalyst, corresponding to (011) lattice plane of La$_2$O$_3$ and (002) lattice plane of SrO, respectively. The EDS elemental mapping images (Fig. S3c and Fig. 1e-h) of LaNiO$_{3-\delta}$-600H$_2$ and La$_{0.5}$Sr$_{0.5}$NiO$_{3-\delta}$-600H$_2$ exhibited the uniform distribution of Ni and other elements. However, a further increase of Sr content led to serious agglomeration of Ni nanoparticles (Fig. S4-S5c).

Fig. 2a and Fig. S6 showed the temperature dependence of NH$_3$ conversion rate of Ni-based catalysts for the ammonia decomposition with a GHSV of 30,000 mL·g_{cat}^{-1}·h^{-1}. The catalytic performance was closely related to the content of Sr and La$_{0.5}$Sr$_{0.5}$NiO$_{3-\delta}$-600H$_2$ exhibited excellent activity with the NH$_3$ conversion efficiency of 87.7% at 550 °C, much higher than that of LaNiO$_{3-\delta}$-600H$_2$ (48.7%). Catalysts with other La:Sr ratios (La$_{0.8}$Sr$_{0.2}$NiO$_{3-\delta}$-600H$_2$, La$_{0.67}$Sr$_{0.33}$NiO$_{3-\delta}$-600H$_2$, and La$_{0.33}$Sr$_{0.67}$NiO$_{3-\delta}$-600H$_2$) were also evaluated (Fig. S6), and it was

Table 1
Structure information and catalytic performance over La$_{1-x}$Sr$_x$NiO$_{3-\delta}$-600H$_2$ catalysts.

Catalysts	Size of Ni nanoparticles (nm)[a]	Specific surface area (m^2/g)[b]	Rate at 550 °C (mmol$_{H2}$·g_{cat}^{-1}·min^{-1})	E$_a$ (kJ/mol)
LaNiO$_{3-\delta}$-600H$_2$	8.5 ± 2.0	13.93	16.3	85.1 ± 0.5
La$_{0.5}$Sr$_{0.5}$NiO$_{3-\delta}$-600H$_2$	13.7 ± 3.4	12.40	29.4	97.2 ± 0.6
La$_{0.2}$Sr$_{0.8}$NiO$_{3-\delta}$-600H$_2$	22.7 ± 4.7	11.33	22.3	104.7 ± 2.2
SrNiO$_{3-\delta}$-600H$_2$	35.0 ± 8.4	9.01	16.4	106.4 ± 2.1

[a]TEM results. [b]Specific surface area was calculated based on N$_2$ adsorption-desorption.

found that their catalytic activity was close to that of La$_{0.5}$Sr$_{0.5}$NiO$_{3-\delta}$-600H$_2$. However, the further increase of Sr content decreased the catalytic activity (The conversion rate of ammonia for La$_{0.2}$Sr$_{0.8}$NiO$_{3-\delta}$-600H$_2$ and SrNiO$_{3-\delta}$-600H$_2$ catalysts was 66.5 and 48.9% at 550 °C, respectively). These results proved that appropriate amount of Sr could promote hydrogen production from ammonia decomposition. In addition, to check the effect of reduction temperature on the catalytic performance, meanwhile, considering the highest test temperature, the La$_{0.5}$Sr$_{0.5}$NiO$_{3-\delta}$ was reduced at higher temperatures above 600 °C, i.e. 700 °C and 800 °C. However, higher reduction temperature resulted in Ni agglomeration (Fig. S7a-f), and decreased catalytic activity (Fig. S7h), which was most likely due to oversized Ni nanoparticles hindering the exposure of active sites. According to the effect of reduction temperature and catalyst composition on catalytic performance, and in order to better uncover the structure-function relationship of catalysts, LaNiO$_{3-\delta}$-600H$_2$, La$_{0.5}$Sr$_{0.5}$NiO$_{3-\delta}$-600H$_2$,

Table 2
Comparison of catalytic performance with other Ni-based catalysts.

Catalysts	Ni (wt%)	Temperature (°C)	GHSV (mL·g$_{cat}^{-1}$·h^{-1})	Conv. (%)	Yield (mmol$_{H2}$·g$_{cat}^{-1}$·min^{-1})	Reference
LaNiO$_{3-\delta}$-600H$_2$	25.5	550	30,000	48.7	16.3	This study
La$_{0.5}$Sr$_{0.5}$NiO$_{3-\delta}$-600H$_2$	25.6	550	30,000	87.7	29.4	This study
La$_{0.2}$Sr$_{0.8}$NiO$_{3-\delta}$-600H$_2$	26.8	550	30,000	66.5	22.3	This study
SrNiO$_{3-\delta}$-600H$_2$	28.6	550	30,000	48.9	16.4	This study
Ni$_x$(Mg$_y$Al$_z$O$_n$)	40.1	600	30,000	99.3	33.3	[51]
4Ni/Ce$_{0.8}$Zr$_{0.2}$O$_2$-SA	13.2	550	3600	95.7	3.7	[52]
Ni/La$_2$O$_3$	40	550	6000	78.9	4.8	[53]
40Ni/5MgLa	40	550	30,000	82.0	27.1	[54]
Ni/CeO$_2$-BN	10	550	30,000	63.0	21.1	[17]
20Ni/Al$_1$Ce$_{0.05}$O$_x$	20	500	30,000	50.8	17.0	[55]
20Ni/La-MgO	20	500	22,000	82.0	21.0	[16]
Ni$_{10}$Ce$_5$O$_x$/Al$_2$O$_3$	17	525	30,000	75.0	25.1	[20]
Ni$_1$/C-LDHs-ST	23.6	550	30,000	53.0	16.3	[56]
Ni/ZSM-5	5	550	30,000	64.0	21.4	[57]
Ni@SiO$_2$	-	500	30,000	36	12.0	[58]
Ni/Al$_2$O$_3$	-	450	30,000	15	4.8	[59]
Ni/La-Al$_2$O$_3$	-	450	30,000	26	8.7	[59]
Ni/CNTs	-	500	30,000	9	3.0	[60]
Ni/SBA-15	23.4	550	30,000	89	29.8	[61]
Ni/SiO$_2$-Al$_2$O$_3$	65	450	30,000	9	3.0	[62]
Ni-50/ATP	38.6	650	30,000	89.9	30.1	[63]
Ni/MCM-41	5	500	30,000	11	3.7	[64]
Ni/OMC	10	500	30,000	8	2.7	[65]
Ni/GO	10	500	30,000	17	5.7	[65]

La$_{0.2}$Sr$_{0.8}$NiO$_{3-\delta}$-600H$_2$, and SrNiO$_{3-\delta}$-600H$_2$ as main catalysts were studied to reveal the role of Sr promoter. The BET results (Table 1) showed that the specific surface area of catalysts was small, indicating that excellent catalytic activity had little relationship with the specific surface area. Meanwhile, the hydrogen production rates normalized by catalyst mass were calculated at 550 °C (Fig. 2b), and La$_{0.5}$Sr$_{0.5}$NiO$_{3-\delta}$-600H$_2$ achieved the value of 29.4 mmol$_{H2}$·g$_{cat}^{-1}$·min^{-1}, almost twice that of LaNiO$_{3-\delta}$-600H$_2$ and SrNiO$_{3-\delta}$-600H$_2$. Comparable Ni loading amounts of four catalysts (Table S1) suggested that the difference in

catalytic activity should not be related to Ni content in the catalysts. We compared the ammonia decomposition activity of the reported Ni-based catalysts, and found that the La$_{0.5}$Sr$_{0.5}$NiO$_{3-\delta}$-600H$_2$ catalyst displayed excellent performance, which was comparable to the previously reported catalysts as listed in Table 2. The apparent activation energy over catalysts was measured as shown in Fig. 2c. The E$_a$ over the La$_{0.5}$Sr$_{0.5}$NiO$_{3-\delta}$-600H$_2$ catalyst was 97.2 ± 0.6 kJ/mol, lower than that of La$_{0.2}$Sr$_{0.8}$NiO$_{3-\delta}$-600H$_2$ (104.7 ± 2.2 kJ/mol) and SrNiO$_{3-\delta}$-600H$_2$ (106.4 ± 2.1 kJ/mol) but higher than the LaNiO$_{3-\delta}$-600H$_2$ (85.1 ±
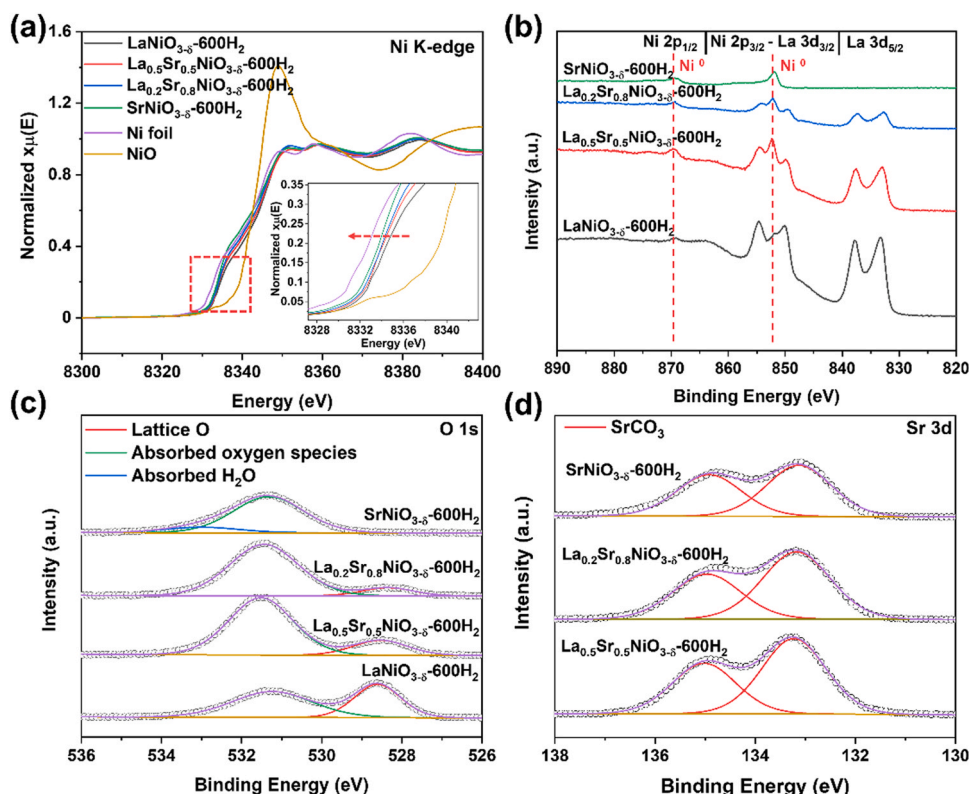

Fig. 3. (a) Ni K edge XANES spectra. *Quasi-in situ* XPS spectra of (b) Ni 2p and La 3d, (c) O 1 s, and (d) Sr 3d.

0.5 kJ/mol). According to the Arrhenius formula (Eq. 7), the reaction rate is not only related to E_a but also to the pre-exponential factor. The $La_{0.5}Sr_{0.5}NiO_{3-\delta}-600H_2$ catalyst had the higher pre-exponential factor, which suggested that the difference in reaction rates was caused by the variation in the number of active sites [20,66,67]. $La_{0.5}Sr_{0.5}NiO_{3-\delta}-600H_2$ catalyst not only had small Ni nanoparticles, but also showed electron-rich nickel species due to its moderate Sr content, which was conducive to fully exposing a large number of highly active electron-rich Ni sites, thus showing higher pre-exponential factor, lower apparent activation energy, and faster reaction rate.

$$k = Ae^{-E_a/RT} \tag{7}$$

The stability of the catalyst is also one of the important aspects to evaluate the catalytic performance. We tested the stability of $La_{0.5}Sr_{0.5}NiO_{3-\delta}-600H_2$ for 48 hours at 550 °C with a GHSV of 30,000 mL·g_{cat}^{-1}·h^{-1}. The results revealed that the NH_3 conversion rate of $La_{0.5}Sr_{0.5}NiO_{3-\delta}-600H_2$ remained around 85% without deactivation (Fig. 2d), demonstrating outstanding stability. The morphology and structure of catalysts after the reaction were analyzed by TEM and XRD (Fig. S9-S12). For the used $La_{0.5}Sr_{0.5}NiO_{3-\delta}-600H_2$ catalyst, the size of Ni nanoparticles did not increase and no aggregation was observed in the EDS elemental mapping images (Fig. S9a,b). In addition, there was no significant change in the XRD patterns of $La_{0.5}Sr_{0.5}NiO_{3-\delta}-600H_2$ after the reaction (Fig. S9c). These results further demonstrated excellent stability of the $La_{0.5}Sr_{0.5}NiO_{3-\delta}-600H_2$ catalyst. Nevertheless, Ni nanoparticles of the used $La_{0.2}Sr_{0.8}NiO_{3-\delta}-600H_2$ and $SrNiO_{3-\delta}$-600H_2 increased from 22.7 ± 4.7 nm to 26.3 ± 6.9 nm and 35.0 ± 8.4 nm to 38.3 ± 11.7 nm (Fig. S11a and S12a), respectively. The EDS elemental mapping images displayed that Ni nanoparticles of the used $La_{0.2}Sr_{0.8}NiO_{3-\delta}-600H_2$ and $SrNiO_{3-\delta}$-600H_2 aggregated after the reaction (Fig. S11b and S12b). Meanwhile, the phase structure of $La_{0.2}Sr_{0.8}NiO_{3-\delta}-600H_2$ and $SrNiO_{3-\delta}$-600H_2 also changed significantly after the reaction (Fig. S11c and S12c). In contrast, the size of Ni species and phase structure for used $LaNiO_{3-\delta}$-600H_2 remained as displayed in Fig. S10a-c. These evidences indicated that the stability of catalysts decreased with a further increase of Sr content and the La_2O_3 inhibited Ni nanoparticles sintering.

It is generally considered that recombination and desorption of nitrogen is the rate-determining step during the ammonia decomposition reaction [18,20], and the electron-enriched active metal is conducive to this step [17]. Alkali metals and alkaline earth metals are often used as electron promoters to change the electronic structure of the active metal, and regulate the adsorption of the intermediate species during the reaction to improve the catalytic performance. Here, SrO might act as both the support and the promoter to affect catalytic activity. To verify the effect of the Sr electron promoter, XANES and XPS were used to analyze the electron structure of Ni species. The normalized Ni K-edge XANES spectra of various catalysts, standard NiO, and Ni foil were shown in Fig. 3a and its inset. The Ni species of all catalysts with relatively large particle sizes looked similar to the standard Ni foil, with an edge near 8333 eV [38,68], suggesting that the Ni species was solely in the metallic state, despite of their particle sizes varying from 8.5 to 35 nm. Besides, with the increase of Sr content, the energy at the Ni K-edge was redshifted, revealing that the introduction of Sr increased the electron density of Ni (the inset of Fig. 3a), which would facilitate the recombination and desorption of nitrogen.

XPS was used to analyze the composition and surface information of the catalysts. For the *ex-situ* XPS spectra, the overlap of the Ni 2$p_{3/2}$ and La 3$d_{3/2}$ made the analysis of XPS results difficult [69]. Nonetheless, peaks of Ni^0 are usually easy to be identified. As shown in Fig. S13a, the peaks at 834.4 and 838.4 eV corresponded to La 3$d_{5/2}$, and the La 3$d_{3/2}$ signal showed bands at 851.4 and 855.3 eV. The four peaks were attributed to the La^{3+} oxidation state [70]. However, no signals of the Ni^0 were observed, possibly the surface of metal nickel was oxidized due to exposure to air. There are usually three peaks in the O 1 s spectra [38,
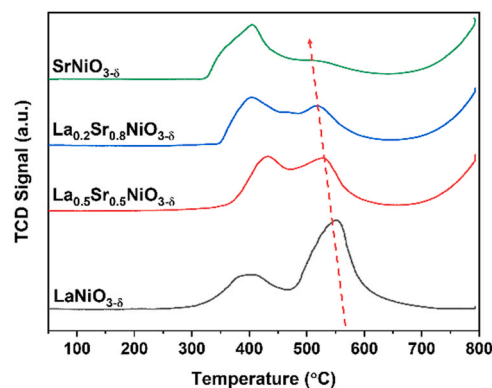

Fig. 4. H$_2$-TPR profiles of the $La_{1-x}Sr_xNiO_{3-\delta}$.

41]: the first peak around 529 eV can be attributed to O^{2-} in the crystal lattice, the peak around 531 eV belongs to the adsorbed oxygen species (hydroxyls and carbonate species), and the peak around 533 eV is distinguished into the adsorbed water. The O 1 s spectra of the catalysts (Fig. S13b) suggested that the oxygen species of $LaNiO_{3-\delta}$-600H_2 was mainly composed of lattice oxygen and adsorbed oxygen species. Whereas, the lattice oxygen decreased and adsorbed oxygen species correspondingly increased with improving Sr content. A possible reason was that as an alkaline earth metal oxide, SrO easily absorbed CO_2 from the air to form carbonate, and XPS is a surface analysis characterization. For the Sr 3d spectra of catalysts, the Sr 3$d_{5/2}$ peak at 133.5 eV could be assigned to strontium carbonate species (Fig. S13c) [71], which was consistent with the higher proportion of adsorbed oxygen species in O 1 s spectra for Sr-containing catalysts. However, the *ex-situ* XPS results could not reflect the real surface structure information of the catalysts under reaction conditions. Thus, *quasi-in situ* XPS was used to reveal a more real catalyst state. For the Ni 2p and La 3d region (Fig. 3b), in addition to the four peaks belonging to La^{3+}, the other two peaks around 852.3 and 869.7 eV were observed, which could be attributed to 2$p_{3/2}$ and 2$p_{1/2}$ of Ni^0 [69], respectively. Compared to *ex-situ* XPS spectra, the observation of metallic Ni in *quasi-in situ* XPS spectra indicated that Ni species was reduced to Ni^0 under reaction conditions, which was considered to be the active species for the ammonia decomposition reaction [16]. The information provided by O 1 s and Sr 3d spectra in *quasi in-situ* XPS (Fig. 3c, d) was similar to that exhibited by *ex-situ* XPS.

The reducibility of the catalysts was explored using H_2-TPR tests (Fig. 4), which could distinguish Ni sites in different chemical environments. The $LaNiO_{3-\delta}$ ($LaNiO_3$ perovskite) exhibited two main reduction peaks in the 300–450 °C and 500–600 °C temperature ranges, respectively. The first reduction peak was attributed to the reduction of Ni^{3+} in $LaNiO_3$ to Ni^{2+} in $La_2Ni_2O_5$, while the second reduction peak at a higher temperature was related to the complete reduction of Ni^{2+} in $La_2Ni_2O_5$ to Ni^0 in metallic nickel [36,38,41]. For the other three catalysts containing Sr, there were also two main reduction peaks and the second peak corresponding to the reduction of nickel species to Ni^0 moved to the lower temperature with the increase of Sr content. Combined with XRD patterns (Fig. S1) and TEM images (Fig. 1 and Fig. S3-S5), these results suggested that the introduction of Sr destroyed the structure of the ABO$_3$ perovskite phase and made it easier for Ni species to be reduced, resulting in the generation of larger metallic Ni nanoparticles. And the size of Ni nanoparticles would further increase with greater Sr content under the same reduction conditions. However, the large size of metal nanoparticles is not conducive to the exposure of active sites. Thus, $La_{0.2}Sr_{0.8}NiO_{3-\delta}-600H_2$ and $SrNiO_{3-\delta}$-600H_2 exhibited lower catalytic activity than $La_{0.5}Sr_{0.5}NiO_{3-\delta}-600H_2$.

In situ DRIFTS spectra under a 10% NH_3/He atmosphere with a temperature range of 50–450 °C at a step of 50 °C were performed to explore the intermediate species during the reaction (Fig. 5). After the NH_3 flow was purged, the obvious vibration peaks at 1626 cm^{-1}
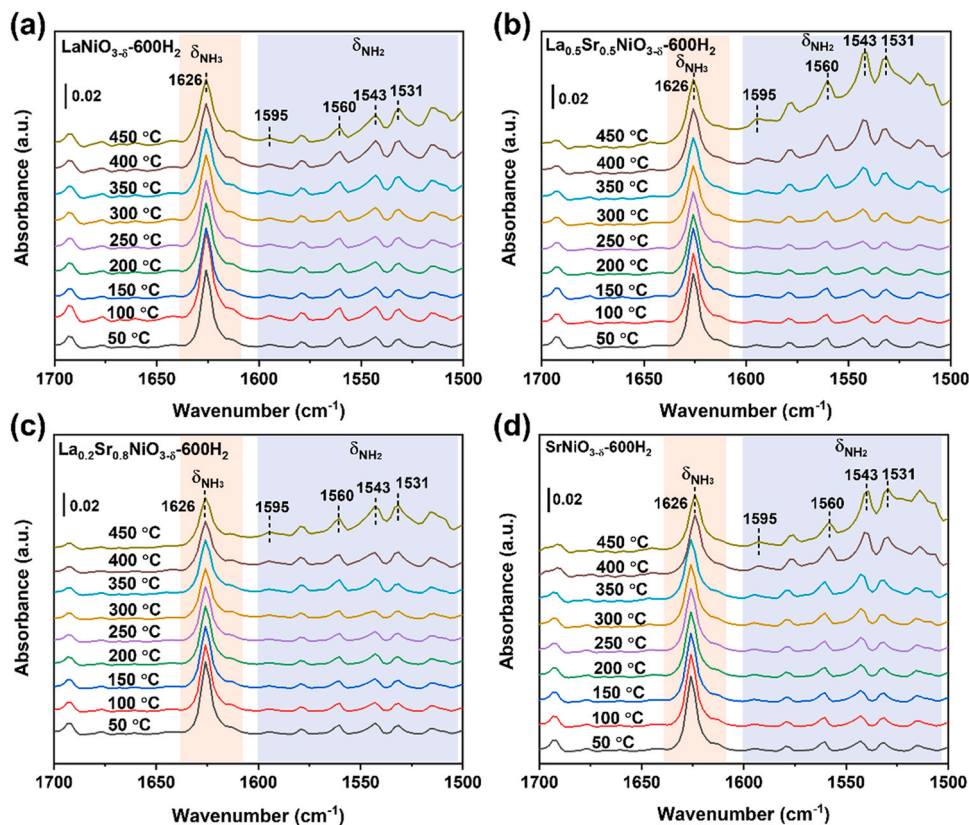
Fig. 5. *In situ* DRIFTS spectra of the steady-state mode under 10% NH_3/He of (a) $LaNiO_{3-\delta}$-600H_2, (b) $La_{0.5}Sr_{0.5}NiO_{3-\delta}-600H_2$, (c) $La_{0.2}Sr_{0.8}NiO_{3-\delta}-600H_2$, and (d) $SrNiO_{3-\delta}$-600H_2.
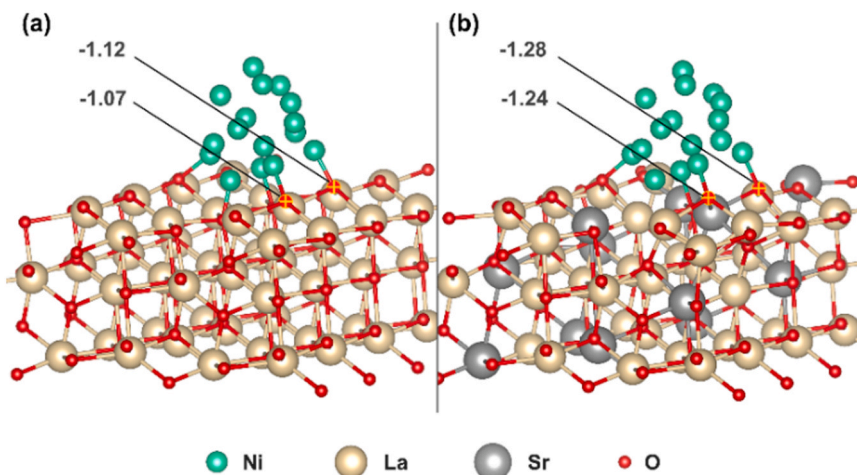
Fig. 6. Structural models and the Hirshfeld charge of several O atoms for (a) Ni/La_2O_3 and (b) $Ni/Sr-La_2O_3$.

corresponding to NH_3 appeared and the *NH_2 species was observed at wavenumbers of 1595, 1560, 1543, and 1531 cm^{-1} over various catalysts [20,22,72]. With the temperature increasing, the absorption intensity of peaks belonging to dissociated *NH_2 became stronger and that of the $La_{0.5}Sr_{0.5}NiO_{3-\delta}-600H_2$ catalyst was stronger compared to the other three catalysts. The results of *in situ* DRIFTS profiles indicated the synergistic effect between SrO and La_2O_3 in improving the catalytic performance of the $La_{0.5}Sr_{0.5}NiO_{3-\delta}-600H_2$ catalyst.

To deeply unravel the influence of Sr, DFT calculations were further performed on Ni/La_2O_3 and $Ni/Sr-La_2O_3$ with optimized structural models (Fig. 6). Throughout the calculations, we found that the O atoms bonded with both Sr and Ni atoms of $Ni/Sr-La_2O_3$ had more negative Hirshfeld charge, thus showing stronger alkalinity [73]. The average Hirshfeld charge of the O atoms was also calculated, and that of $Ni/Sr-La_2O_3$ was more negative than Ni/La_2O_3 (Table S4). Experimentally, CO_2-TPD (Fig. S16) was carried out to reveal the alkalinity of catalysts. Compared to the $LaNiO_{3-\delta}$-600H_2, $La_{0.5}Sr_{0.5}NiO_{3-\delta}-600H_2$ exhibited a strong CO_2 desorption peak at about 900 °C, attributed to strong base sites, which was consistent with DFT calculations. These results demonstrated that the Sr as the promoter increased the alkalinity of supports, and the Ni species was situated in a more electro-negative environment such that the rate-determining step of ammonia decomposition reaction was accelerated.

4. Conclusion

In summary, La$_{1-x}$Sr$_x$NiO$_{3-\delta}$-600H$_2$ catalysts were obtained by reducing the oxide precursors derived from the substitution of the 'A-site' in LaNiO$_3$ by Sr cations, in which La$_{0.5}$Sr$_{0.5}$NiO$_{3-\delta}$-600H$_2$ showed excellent catalytic performance in ammonia decomposition reaction. It was found that the ammonia decomposition activity showed a close correlation with the content of Sr. On the one hand, according to the XRD, TEM, and H$_2$-TPR, the introduction of Sr facilitated the reduction of Ni species, resulting in the formation of larger Ni nanoparticles, which was not conducive to the exposure of active sites, while La$_2$O$_3$ guaranteed better dispersion of nickel species. On the other hand, XANES, CO$_2$-TPD, and DFT calculations suggested that the alkalinity of catalysts and electron density of the active metal was enhanced by Sr as the electron promoter, thus speeding up the recombination and desorption of nitrogen. Finally, the two factors reached a balance on the La$_{0.5}$Sr$_{0.5}$NiO$_{3-\delta}$-600H$_2$ catalyst, thus showing outstanding catalytic activity. This study has provided a fresh way to construct and optimize efficient heterogeneous catalysts by modulating the electron density of active metals with alkaline earth metal promoters.

CRediT authorship contribution statement

Ya-Wen Zhang: Writing – review & editing, Supervision, Conceptualization. **Chen Li:** Visualization, Supervision, Software. **Chun-Jiang Jia:** Resources, Investigation, Conceptualization. **Hao Dong:** Supervision, Conceptualization. **Ting-Zhou Li:** Data curation. **Qian Zhang:** Data curation. **Jun-Hao Wang:** Visualization, Software. **Xiao-Yu Guo:** Writing – original draft, Methodology, Investigation, Formal analysis, Data curation, Conceptualization.

Declaration of Competing Interest

The authors declare that they have no known competing financial interests or personal relationships that could have appeared to influence the work reported in this paper.

Data availability

Data will be made available on request.

Acknowledgement

Appendix A. Supporting information

Supplementary data associated with this article can be found in the online version at doi:10.1016/j.apcatb.2024.123844.

References

[1] J. Guo, P. Chen, Catalyst: NH$_3$ as an energy carrier, Chem 3 (2017) 709–712, https://doi.org/10.1016/j.chempr.2017.10.004.

[2] S. Mukherjee, S.V. Devaguptapu, A. Sviripa, C.R.F. Lund, G. Wu, Low-temperature ammonia decomposition catalysts for hydrogen generation, Appl. Catal., B 226 (2018) 162–181, https://doi.org/10.1016/j.apcatb.2017.12.039.

[3] I. Lucentini, X. Garcia, X. Vendrell, J. Llorca, Review of the decomposition of ammonia to generate hydrogen, Ind. Eng. Chem. Res. 60 (2021) 18560–18611, https://doi.org/10.1021/acs.iecr.1c00843.

[4] Y. Zhou, X. Peng, T. Zhang, H. Cai, B. Lin, L. Zheng, X. Wang, L. Jiang, Essential role of Ru–anion interaction in Ru-based ammonia synthesis catalysts, ACS Catal. 12 (2022) 7633–7642, https://doi.org/10.1021/acscatal.2c01486.

[5] H. Fang, Y. Zhou, X. Peng, Y. Luo, X. Wang, S. Liang, L. Jiang, Challenges and prospects in artificial nitrogen cycle for energy decarbonization, Natl. Sci. Open 2 (2023) 20220040, https://doi.org/10.1360/nso/20220040.

[6] J.C. Ganley, F.S. Thomas, E.G. Seebauer, R.I. Masel, A priori catalytic activity correlations: the difficult case of hydrogen production from ammonia, Catal. Lett. 96 (2004) 117–122, https://doi.org/10.1023/B:CATL.0000030108.50691.d4.

[7] S. Kang, J. Cha, Y. Jo, Y. Lee, H. Sohn, Y. Song, Y. Kim, D. Lim, J. Park, C. Yoon, Heteroepitaxial growth of B$_5$-site-rich Ru nanoparticles guided by hexagonal boron nitride for low-temperature ammonia dehydrogenation, Adv. Mater. 35 (2023) 2203364, https://doi.org/10.1002/adma.202203364.

[8] H. Fang, S. Wu, T. Ayvali, J. Zheng, J. Fellowes, P.-L. Ho, K.C. Leung, A. Large, G. Held, R. Kato, K. Suenaga, Y.I.A. Reyes, H.V. Thang, H.-Y.T. Chen, S.C.E. Tsang, Dispersed surface Ru ensembles on MgO(111) for catalytic ammonia decomposition, Nat. Commun. 14 (2023) 647, https://doi.org/10.1038/s41467-023-36339-w.

[9] K.C. Leung, S. Hong, G. Li, Y. Xing, B.K.Y. Ng, P. Ho, D. Ye, P. Zhao, E. Tan, O. Safonova, T. Wu, M.M.-J. Li, G. Mpourmpakis, S.C.E. Tsang, Confined Ru sites in a 13X zeolite for ultrahigh H$_2$ production from NH$_3$ decomposition, J. Am. Chem. Soc. 145 (2023) 14548–14561, https://doi.org/10.1021/jacs.3c05092.

[10] C. Mao, J. Wang, Y. Zou, G. Qi, J.Y. Yang Loh, T. Zhang, M. Xia, J. Xu, F. Deng, M. Ghoussoub, N.P. Kherani, L. Wang, H. Shang, M. Li, J. Li, X. Liu, Z. Ai, G. A. Ozin, J. Zhao, L. Zhang, Hydrogen spillover to oxygen vacancy of TiO$_{2-x}$H$_y$/Fe: breaking the scaling relationship of ammonia synthesis, J. Am. Chem. Soc. 142 (2020) 17403–17412, https://doi.org/10.1021/jacs.0c06118.

[11] J. Humphreys, R. Lan, S. Chen, M. Walker, Y. Han, S. Tao, Cation doped cerium oxynitride with anion vacancies for Fe-based catalyst with improved activity and oxygenate tolerance for efficient synthesis of ammonia, Appl. Catal., B 285 (2021) 119843, https://doi.org/10.1016/j.apcatb.2020.119843.

[12] M. Hattori, N. Okuyama, H. Kurosawa, M. Hara, Low-temperature ammonia synthesis on iron catalyst with an electron donor, J. Am. Chem. Soc. 145 (2023) 7888–7897, https://doi.org/10.1021/jacs.2c13015.

[13] G. Han, F. Li, Z. Chen, C. Coppex, S. Kim, H. Noh, Z. Fu, Y. Lu, C.V. Singh, S. Siahrostami, Q. Jiang, J. Baek, Mechanochemistry for ammonia synthesis under mild conditions, Nat. Nanotechnol. 16 (2021) 325–330, https://doi.org/10.1038/s41565-020-00809-9.

[14] L. Huo, B. Liu, H. Li, B. Cao, X. Hu, X. Fu, C. Jia, J. Zhang, Component synergy and armor protection induced superior catalytic activity and stability of ultrathin Co-Fe spinel nanosheets confined in mesoporous silica shells for ammonia decomposition reaction, Appl. Catal., B 253 (2019) 121–130, https://doi.org/10.1016/j.apcatb.2019.04.053.

[15] B. Lorenzut, T. Montini, M. Bevilacqua, P. Fornasiero, FeMo-based catalysts for H$_2$ production by NH$_3$ decomposition, Appl. Catal. B 125 (2012) 409–417, https://doi.org/10.1016/j.apcatb.2012.06.011.

[16] X. Hu, W. Wang, Z. Jin, X. Wang, R. Si, C. Jia, Transition metal nanoparticles supported La-promoted MgO as catalysts for hydrogen production via catalytic decomposition of ammonia, J. Energy Chem. 38 (2019) 41–49, https://doi.org/10.1016/j.jechem.2018.12.024.

[17] C. Zhou, K. Wu, H. Huang, C. Cao, Y. Luo, C. Chen, L. Lin, C. Au, L. Jiang, Spatial confinement of electron-rich Ni nanoparticles for efficient ammonia decomposition to hydrogen production, ACS Catal. 11 (2021) 10345–10350, https://doi.org/10.1021/acscatal.1c02420.

[18] H. Tabassum, S. Mukherjee, J. Chen, D. Holiharimanana, S. Karakalos, X. Yang, S. Hwang, T. Zhang, B. Lu, M. Chen, Z. Tang, E.A. Kyriakidou, Q. Ge, G. Wu, Hydrogen generation via ammonia decomposition on highly efficient and stable Ru-free catalysts: approaching complete conversion at 450 °C, Energy Environ. Sci. 15 (2022) 4190–4200, https://doi.org/10.1039/D1EE03730G.

[19] I. Lucentini, G. García Colli, C.D. Luzi, I. Serrano, O.M. Martínez, J. Llorca, Catalytic ammonia decomposition over Ni-Ru supported on CeO$_2$ for hydrogen production: effect of metal loading and kinetic analysis, Appl. Catal. B 286 (2021) 119896, https://doi.org/10.1016/j.apcatb.2021.119896.

[20] L. Zhou, X. Fu, Y. Xu, W. Wang, C. Jia, Constructing efficient nickel catalysts on CeO$_x$ nanoparticles stabilized using γ-Al$_2$O$_3$ to catalyze ammonia decomposition for hydrogen production, ACS Appl. Nano Mater. 6 (2023) 2952–2962, https://doi.org/10.1021/acsanm.2c05345.

[21] T.A. Le, Y. Kim, H.W. Kim, S. Lee, J. Kim, T. Kim, Y. Lee, H. Chae, Ru-supported lanthania-ceria composite as an efficient catalyst for CO$_x$-free H$_2$ production from ammonia decomposition, Appl. Catal., B 285 (2021) 119831, https://doi.org/10.1016/j.apcatb.2020.119831.

[22] X. Hu, X. Fu, W. Wang, X. Wang, K. Wu, R. Si, C. Ma, C. Jia, C. Yan, Ceria-supported ruthenium clusters transforming from isolated single atoms for hydrogen production via decomposition of ammonia, Appl. Catal. B 268 (2020) 118424, https://doi.org/10.1016/j.apcatb.2019.118424.

[23] S.J. Wang, S.F. Yin, L. Li, B.Q. Xu, C.F. Ng, C.T. Au, Investigation on modification of Ru/CNTs catalyst for the generation of CO$_x$-free hydrogen from ammonia, Appl. Catal. B 52 (2004) 287–299, https://doi.org/10.1016/j.apcatb.2004.05.002.

[24] A.K. Hill, L. Torrente-Murciano, In-situ H$_2$ production via low temperature decomposition of ammonia: insights into the role of cesium as a promoter, Int. J. Hydrog. Energy 39 (2014) 7646–7654, https://doi.org/10.1016/j.ijhydene.2014.03.043.

[25] K. Yang, Y. Zhang, Y. Li, P. Huang, X. Chen, W. Dai, X. Fu, Insight into the function of alkaline earth metal oxides as electron promoters for Au/TiO$_2$ catalysts used in CO oxidation, Appl. Catal. B 183 (2016) 206–215, https://doi.org/10.1016/j.apcatb.2015.10.046.

[26] C. Huang, Y. Yu, J. Yang, Y. Yan, D. Wang, F. Hu, X. Wang, R. Zhang, G. Feng, Ru/ La₂O₃ catalyst for ammonia decomposition to hydrogen, Appl. Surf. Sci. 476 (2019) 928–936, https://doi.org/10.1016/j.apsusc.2019.01.112.

[27] K. Nagaoka, T. Eboshi, N. Abe, S. Miyahara, K. Honda, K. Sato, Influence of basic dopants on the activity of Ru/Pr₆O₁₁ for hydrogen production by ammonia decomposition, Int. J. Hydrog. Energy 39 (2014) 20731–20735, https://doi.org/10.1016/j.ijhydene.2014.07.142.

[28] X. Ju, L. Liu, P. Yu, J. Guo, X. Zhang, T. He, G. Wu, P. Chen, Mesoporous Ru/MgO prepared by a deposition-precipitation method as highly active catalyst for producing CO₂-free hydrogen from ammonia decomposition, Appl. Catal. B 211 (2017) 167–175, https://doi.org/10.1016/j.apcatb.2017.04.043.

[29] Y. Gu, Z. Jin, H. Zhang, R.-J. Xu, M. Zheng, Y. Guo, Q. Song, C. Jia, Transition metal nanoparticles dispersed in an alumina matrix as active and stable catalysts for CO₂-free hydrogen production from ammonia, J. Mater. Chem. A 3 (2015) 17172–17180, https://doi.org/10.1039/C5TA04179A.

[30] T.S. Galhardo, A.H. Braga, B.H. Arpini, J. Szanyi, R.V. Gonçalves, B.F. Zornio, C. R. Miranda, L.M. Rossi, Optimizing active sites for high CO selectivity during CO₂ hydrogenation over supported nickel catalysts, J. Am. Chem. Soc. 143 (2021) 4268–4280, https://doi.org/10.1021/jacs.0c12689.

[31] R.A. Ortega-Domínguez, H. Vargas-Villagrán, C. Peñaloza-Orta, K. Saavedra-Rubio, X. Bokhimi, T.E. Klimova, A facile method to increase metal dispersion and hydrogenation activity of Ni/SBA-15 catalysts, Fuel 198 (2017) 110–122, https://doi.org/10.1016/j.fuel.2016.12.037.

[32] Y. Ren, Y. Yang, M. Wei, Recent advances on heterogeneous non-noble metal catalysts toward selective hydrogenation reactions, ACS Catal. 13 (2023) 8902–8924, https://doi.org/10.1021/acscatal.3c01442.

[33] V. Deerattrakul, P. Dittanet, M. Sawangphruk, P. Kongkachuichay, CO₂ hydrogenation to methanol using Cu-Zn catalyst supported on reduced graphene oxide nanosheets, J. CO₂ Util. 16 (2016) 104–113, https://doi.org/10.1016/j.jcou.2016.07.002.

[34] R.J. da Silva, A.F. Pimentel, R.S. Monteiro, C.J.A. Mota, Synthesis of methanol and dimethyl ether from the CO₂ hydrogenation over Cu·ZnO supported on Al₂O₃ and Nb₂O₅, J. CO₂ Util. 15 (2016) 83–88, https://doi.org/10.1016/j.jcou.2016.01.006.

[35] Y. Nishihata, J. Mizuki, T. Akao, H. Tanaka, M. Uenishi, M. Kimura, T. Okamoto, N. Hamada, Self-regeneration of a Pd-perovskite catalyst for automotive emissions control, Nature 418 (2002) 164–167, https://doi.org/10.1038/nature00893.

[36] M. Pinzón, A. Sánchez-Sánchez, P. Sánchez, A.R. de la Osa, A. Romero, Ammonia as a carrier for hydrogen production by using lanthanum based perovskites, Energy Convers. Manag. 246 (2021) 114681, https://doi.org/10.1016/j.enconman.2021.114681.

[37] P. Steiger, R. Delmelle, D. Foppiano, L. Holzer, A. Heel, M. Nachtegaal, O. Kröcher, D. Ferri, Structural reversibility and nickel particle stability in lanthanum iron nickel perovskite-type catalysts, ChemSusChem 10 (2017) 2505–2517, https://doi.org/10.1002/cssc.201700358.

[38] S. Das, S. Bhattar, L. Liu, Z. Wang, S. Xi, J.J. Spivey, S. Kawi, Effect of partial Fe substitution in La₀.₉Sr₀.₁NiO₃ perovskite-derived catalysts on the reaction mechanism of methane dry reforming, ACS Catal. 10 (2020) 12466–12486, https://doi.org/10.1021/acscatal.0c01229.

[39] S. Shah, J. Hong, L. Cruz, S. Wasantwisut, S.R. Bare, K.L. Gilliard-AbdulAziz, Dynamic tracking of NiFe smart catalysts using in situ X-Ray absorption spectroscopy for the dry methane reforming reaction, ACS Catal. 13 (2023) 3990–4002, https://doi.org/10.1021/acscatal.2c05572.

[40] C.W. Thurner, N. Bonmassar, D. Winkler, L. Haug, K. Ploner, P. Delir Kheyrollahi Nezhad, X. Drexler, A. Mohammadi, P.A. van Aken, J. Kunze-Liebhäuser, A. Niaei, J. Bernardi, B. Klötzer, S. Penner, Who does the job? How copper can replace noble metals in sustainable catalysis by the formation of copper–mixed oxide interfaces, ACS Catal. 12 (2022) 7696–7708, https://doi.org/10.1021/acscatal.2c01584.

[41] K. Sutthiumporn, T. Maneerung, Y. Kathiraser, S. Kawi, CO₂ dry-reforming of methane over La₀.₈Sr₀.₂Ni₀.₈M₀.₂O₃ perovskite (M = Bi, Co, Cr, Cu, Fe): roles of lattice oxygen on C–H activation and carbon suppression, Int. J. Hydrog. Energy 37 (2012) 11195–11207, https://doi.org/10.1016/j.ijhydene.2012.04.059.

[42] M.A. Peña, J.L.G. Fierro, Chemical structures and performance of perovskite oxides, Chem. Rev. 101 (2001) 1981–2018, https://doi.org/10.1021/cr980129f.

[43] M.R. Goldwasser, M.E. Rivas, M.L. Lugo, E. Pietri, J. Pérez-Zurita, M.L. Cubeiro, A. Griboval-Constant, G. Leclercq, Combined methane reforming in presence of CO₂ and O₂ over LaFe₁₋ₓCoₓO₃ mixed-oxide perovskites as catalysts precursors, Catal. Today 107-108 (2005) 106–113, https://doi.org/10.1016/j.cattod.2005.07.073.

[44] G. Kresse, J. Furthmüller, Efficient iterative schemes for ab initio total-energy calculations using a plane-wave basis set, Phys. Rev. B 54 (1996) 11169–11186, https://doi.org/10.1103/PhysRevB.54.11169.

[45] G. Kresse, J. Furthmüller, Efficiency of ab-initio total energy calculations for metals and semiconductors using a plane-wave basis set, Comput. Mater. Sci. 6 (1996) 15–50, https://doi.org/10.1016/0927-0256(96)00008-0.

[46] G. Kresse, D. Joubert, From ultrasoft pseudopotentials to the projector augmented-wave method, Phys. Rev. B 59 (1999) 1758–1775, https://doi.org/10.1103/PhysRevB.59.1758.

[47] V. Wang, N. Xu, J.-C. Liu, G. Tang, W.-T. Geng, VASPKIT: a user-friendly interface facilitating high-throughput computing and analysis using VASP code, Comput. Phys. Commun. 267 (2021) 108033, https://doi.org/10.1016/j.cpc.2021.108033.

[48] A.N. Grundy, B. Hallstedt, L.J. Gauckler, Experimental phase diagram determination and thermodynamic assessment of the La₂O₃–SrO system, Acta Mater. 50 (2002) 2209–2222, https://doi.org/10.1016/S1359-6454(01)00432-3.

[49] L. Cong, Y. Zhao, S. Li, Y. Sun, Sr-doping effects on La₂O₃ catalyst for oxidative coupling of methane, Chin. J. Catal. 38 (2017) 899–907, https://doi.org/10.1016/S1872-2067(17)62823-7.

[50] J. Song, Y. Sun, R. Ba, S. Huang, Y. Zhao, J. Zhang, Y. Sun, Y. Zhu, Monodisperse Sr–La₂O₃ hybrid nanofibers for oxidative coupling of methane to synthesize C₂ hydrocarbons, Nanoscale 7 (2015) 2260–2264, https://doi.org/10.1039/C4NR06660J.

[51] Q. Su, L. Gu, Y. Yao, J. Zhao, W. Ji, W. Ding, C. Au, Layered double hydroxides derived Niₓ(MgᵧAlₓOₙ) catalysts: enhanced ammonia decomposition by hydrogen spillover effect, Appl. Catal. B 201 (2017) 451–460, https://doi.org/10.1016/j.apcatb.2016.08.051.

[52] Q. Deng, H. Zhang, X. Hou, T. Ren, Z. Yuan, High-surface-area Ce₀.₈Zr₀.₂O₂ solid solutions supported Ni catalysts for ammonia decomposition to hydrogen, Int. J. Hydrog. Energy 37 (2012) 15901–15907, https://doi.org/10.1016/j.ijhydene.2012.08.069.

[53] H. Muroyama, C. Saburi, T. Matsui, K. Eguchi, Ammonia decomposition over Ni/ La₂O₃ catalyst for on-site generation of hydrogen, Appl. Catal. A 443-444 (2012) 119–124, https://doi.org/10.1016/j.apcata.2012.07.031.

[54] Y. Yu, Y. Gan, C. Huang, Z. Lu, X. Wang, R. Zhang, G. Feng, Ni/La₂O₃ and Ni/MgO-La₂O₃ catalysts for the decomposition of NH₃ into hydrogen, Int. J. Hydrog. Energy 45 (2020) 16528–16539, https://doi.org/10.1016/j.ijhydene.2020.04.127.

[55] Q.C. Do, Y. Kim, T.A. Le, G.J. Kim, J. Kim, T. Kim, Y. Lee, H. Chae, Facile one-pot synthesis of Ni-based catalysts by cation-anion double hydrolysis method as highly active Ru-free catalysts for green H₂ production via NH₃ decomposition, Appl. Catal. B 307 (2022) 121167, https://doi.org/10.1016/j.apcatb.2022.121167.

[56] J. Zhao, L. Deng, W. Zheng, S. Xu, Q. Yu, X. Qiu, Nickel-induced structure transformation in hydrocalumite for enhanced ammonia decomposition, Int. J. Hydrog. Energy 45 (2020) 12244–12255, https://doi.org/10.1016/j.ijhydene.2020.02.201.

[57] Z. Hu, C. Weng, C. Chen, Z. Yuan, Catalytic decomposition of ammonia to CO₂-free hydrogen over Ni/ZSM-5 catalysts: a comparative study of the preparation methods, Appl. Catal. A 562 (2018) 49–57, https://doi.org/10.1016/j.apcata.2018.05.038.

[58] L. Yao, T. Shi, Y. Li, J. Zhao, W. Ji, C.-T. Au, Core–shell structured nickel and ruthenium nanoparticles: very active and stable catalysts for the generation of CO₂-free hydrogen via ammonia decomposition, Catal. Today 164 (2011) 112–118, https://doi.org/10.1016/j.cattod.2010.10.056.

[59] J. Zhang, H. Xu, X. Jin, Q. Ge, W. Li, Characterizations and activities of the nano-sized Ni/Al₂O₃ and Ni/La–Al₂O₃ catalysts for NH₃ decomposition, Appl. Catal. A 290 (2005) 87–96, https://doi.org/10.1016/j.apcata.2005.05.020.

[60] S.-F. Yin, Q.-H. Zhang, B.-Q. Xu, W.-X. Zhu, C.-F. Ng, C.-T. Au, Investigation on the catalysis of CO₂-free hydrogen generation from ammonia, J. Catal. 224 (2004) 384–396, https://doi.org/10.1016/j.jcat.2004.03.008.

[61] H. Liu, H. Wang, J. Shen, Y. Sun, Z. Liu, Preparation, characterization and activities of the nano-sized Ni/SBA-15 catalyst for producing CO₂-free hydrogen from ammonia, Appl. Catal. A 337 (2008) 138–147, https://doi.org/10.1016/j.apcata.2007.12.006.

[62] T.V. Choudhary, C. Sivadinarayana, D.W. Goodman, Catalytic ammonia decomposition: CO₂-free hydrogen production for fuel cell applications, Catal. Lett. 72 (2001) 197–201, https://doi.org/10.1023/A:1009023825549.

[63] L. Li, F. Chen, J. Shao, Y. Dai, J. Ding, Z. Tang, Attapulgite clay supported Ni nanoparticles encapsulated by porous silica: Thermally stable catalysts for ammonia decomposition to CO₂ free hydrogen, Int. J. Hydrog. Energy 41 (2016) 21157–21165, https://doi.org/10.1016/j.ijhydene.2016.08.156.

[64] X.-K. Li, W.-J. Ji, J. Zhao, S.-J. Wang, C.-T. Au, Ammonia decomposition over Ru and Ni catalysts supported on fumed SiO₂, MCM-41, and SBA-15, J. Catal. 236 (2005) 181–189, https://doi.org/10.1016/j.jcat.2005.09.030.

[65] T. Meng, Q.-Q. Xu, Y.-T. Li, J.-L. Chang, T.-Z. Ren, Z.-Y. Yuan, Nickle nanoparticles highly dispersed on reduced graphene oxide for ammonia decomposition to hydrogen, J. Ind. Eng. Chem. 32 (2015) 373–379, https://doi.org/10.1016/j.jiec.2015.09.017.

[66] X. Xie, Y. Li, Z. Liu, M. Haruta, W. Shen, Low-temperature oxidation of CO catalysed by Co₃O₄ nanorods, Nature 458 (2009) 746–749, https://doi.org/10.1038/nature07877.

[67] W. Zhang, W. Zhou, Y. Li, J. Ren, Z. Wang, Enhanced ammonia decomposition activity over unsupported Co₃O₄: unravelling the promotion effect of alkali metal, Appl. Catal. B 330 (2023) 122644, https://doi.org/10.1016/j.apcatb.2023.122644.

[68] T. Margossian, K. Larmier, S.M. Kim, F. Krumeich, A. Fedorov, P. Chen, C. R. Müller, C. Copéret, Molecularly tailored nickel precursor and support yield a stable metal dry reforming catalyst with superior metal utilization, J. Am. Chem. Soc. 139 (2017) 6919–6927, https://doi.org/10.1021/jacs.7b01625.

[69] R.C. Rabelo-Neto, H.B.E. Sales, C.V.M. Inocêncio, E. Varga, A. Oszko, A. Erdohelyi, F.B. Noronha, L.V. Mattos, CO₂ reforming of methane over supported LaNiO₃ perovskite-type oxides, Appl. Catal., B 221 (2018) 349–361, https://doi.org/10.1016/j.apcatb.2017.09.022.

[70] C. Chen, R. Bao, L. Yang, S. Tai, Y. Zhao, W. Wang, J. Xia, H. Li, Application of inorganic perovskite LaNiO₃ partial substituted by Ce and Cu in absorbance and photocatalytic degradation of antibiotics, Appl. Surf. Sci. 579 (2022) 152026, https://doi.org/10.1016/j.apsusc.2021.152026.

[71] D.J. Deka, J. Kim, S. Gunduz, D. Jain, Y. Shi, J.T. Miller, A.C. Co, U.S. Ozkan, Coke formation during high-temperature CO₂ electrolysis over AFeO₃ (A = La/Sr)

cathode: effect of A-site metal segregation, Appl. Catal., B 283 (2021) 119642, https://doi.org/10.1016/j.apcatb.2020.119642.

[72] C. Cao, K. Wu, C. Zhou, Y. Yao, Y. Luo, C. Chen, L. Lin, L. Jiang, Electronic metal-support interaction enhanced ammonia decomposition efficiency of perovskite

oxide supported ruthenium, Chem. Eng. Sci. 257 (2022) 117719, https://doi.org/10.1016/j.ces.2022.117719.

[73] F.L. Hirshfeld, Bonded-atom fragments for describing molecular charge densities, Theor. Chim. Acta 44 (1977) 129–138, https://doi.org/10.1007/BF00549096.